ANL/NE-15/26

FASTGRASS Implementation in BISON and Fission Gas Behavior Characterization in UO_2 and Connection to Validating MARMOT

Nuclear Engineering Division

ANL/NE-15/26

FASTGRASS Implementation in BISON and Fission Gas Behavior Characterization in UO_2 and Connection to Validating MARMOT

prepared by
Di Yun, Kun Mo, Bei Ye, Laura M. Jamison and Yinbin Miao
Nuclear Engineering Division, Argonne National Laboratory

Jie Lian and Tiankai Yao
Rensselaer Polytechnic Institute

prepared for
U.S. Department of Energy
Nuclear Energy Advanced Modeling & Simulation Program

September 30, 2015

ABSTRACT

This activity is supported by the US Nuclear Energy Advanced Modeling and Simulation (NEAMS) Fuels Product Line (FPL). Two major accomplishments in FY 15 are summarized in this report: (1) implementation of the FASTGRASS module in the BISON code; and (2) a Xe implantation experiment for large-grained UO_2. Both BISON AND MARMOT codes have been developed by Idaho National Laboratory (INL) to enable next generation fuel performance modeling capability as part of the NEAMS Program FPL. To contribute to the development of the Moose-Bison-Marmot (MBM) code suite, we have implemented the FASTGRASS fission gas model as a module in the BISON code. Based on rate theory formulations, the coupled FASTGRASS module in BISON is capable of modeling LWR oxide fuel fission gas behavior and fission gas release. In addition, we conducted a Xe implantation experiment at the Argonne Tandem Linac Accelerator System (ATLAS) in order to produce the needed UO_2 samples with desired bubble morphology. With these samples, further experiments to study the fission gas diffusivity are planned to provide validation data for the Fission Gas Release Model in MARMOT codes.

CONTENTS

FIGURES

TABLES

1. Introduction

1.1 The Structure and Content of This Report

In this report, we summarize our accomplishments to date in two project areas: (1) implementation of the FASTGRASS module in the BISON code, and (2) Xenon irradiation experiments on large-grained UO_2 samples.

The first chapter of this report introduces the background for each project and summarizes its major achievements.

Chapter 2 describes our development and implementation of the FASTGRASS module in the BISON code. The physics based fission gas behavior and release models and the main rate theory equations are detailed in this chapter.

Chapter 3 provides details of the ion irradiation experiment conducted at the ATLAS at ANL in July 2015. High-energy Xe ions were successfully implanted in four large-grained UO_2 samples. The samples received a dose of 0.79×10^{17} ions/cm^2 at a controlled temperature of ~150ºC. According to SRIM calculation based on the experimental conditions, the peak damage region within the samples reached ~160 dpa. Post-irradiation annealing (PIA) and post-irradiation examinations (PIEs) will be performed on all the irradiated UO_2 samples in FY16. PIA is planned to accelerate bubble formation in the material. The PIEs will include FIB-SEM, TEM, and synchrotron X-ray micro-diffraction examinations.

Finally, Chapter 4 provides a summary of the work conducted in this fiscal year.

1.2 FASTGRASS Implementation in BISON

FASTGRASS is a physics based fission gas behavior and release model which is capable of modeling LWR oxide fuel fission gas behavior and fission gas release. The formation and growth of fission gas bubbles in irradiated nuclear fuels is a process of vital technical importance because the behavior of these gas bubbles can have a significant impact on the swelling of the fuel, which may lead to fuel cladding failure during in-pile irradiation. Fission gas produced within the fuel gets released to the gas plenum which, in turn, causes stress on the cladding materials leading to possible cladding fracture. Because of their technical importance, these issues have been the subject of extensive theoretical (simulation) and experimental investigations [1-4]. Chapter 2 of this report describes and details the implementation of the FASTGRASS fission gas model into the BISON fuel performance code.

Section 2.1 describes the rate theory formulation of the physics based fission gas model. The details of this model, including its benchmarking and validation, can be found in a series of reports by J. Rest [5, 6]. For clarity and completeness, the main rate theory equations are described in full detail in Section 2.2 of this report.

Because of computational efficiency issues, the rate theory formulation of the fission gas model in full detail (as represented in the GRASS-SST code) cannot be directly used in the BISON code. Implementation would cause extremely long run times of the BISON model (the model subroutines need to be called extensively during the fully coupled BISON operations; at fuel center temperatures above 1600˚C, GRASS-SST runs for about 6 minutes per time step on a single CPU). A faster version of the GRASS-SST code, the FASTGRASS code, was therefore utilized for implementation of the fission gas model in the BISON code. According to an earlier study [7], FASTGRASS and GRASS-SST results predicting fission gas release are in agreement. Given the same input parameters, the FASTGRASS model has also produced average gas bubble sizes that are consistent with the average bubble sizes provided by GRASS-SST (note this average is calculated from the detailed bubble size distributions given in GRASS-SST). Bubble number densities calculated by both codes are also in very good agreement. Because the BISON code structure is highly modular in C++ programming language, the FASTGRASS code was translated from its original Fortran 77 form to C++. Individual

computational subroutines were translated separately and tested before they were merged into a standalone operational code. The complete code was then verified by comparing its computational results to the original Fortran 77 form results to ensure consistency.

Section 2.3 describes the implementation of the FASTGRASS fission gas model as a module in the BISON code.

1.3 Xe Implantations on Large-grained UO_2

Chapter 3 of this report describes the Xe irradiation experiment at ATLAS at ANL. This experiment aimed to produce the required bubble structure in large-grained UO_2 samples for further experiments. The final goal of this effort is to provide validation data for the Fission Gas Release Model in MARMOT.

Section 3.1 describes the experimental setup at ATLAS. The irradiation chamber for high-energy ion irradiation was built and installed in the ATLAS beamline in this fiscal year. An advanced sample holder, able to provide closed-loop temperature control and hold up to 19 samples for simultaneous irradiation within a single shot of ion beam, was built and used in the irradiation chamber for Xe implantation in the UO_2 samples.

Section 3.2 provides details of the sample and experimental conditions, including the sample temperature, achieved dose, and Xe concentration levels.

Section 3.3 introduces the detailed plan for the post-irradiation examinations, which include FIB/SEM, TEM, *in-situ* TEM, and synchrotron micro-diffraction. The PIEs will provide direct validation data for the Fission Gas Release Model in MARMOT.

2. FASTGRASS Module Development and Implementation in BISON

2.1 Rate Theory Formulation of Fission Gas Behavior

The analytical models described in this section present a theoretical foundation for the description of fission products in irradiated fuel. Gaseous fission products are responsible for many of the performance characteristics of these fuels. Understanding the interaction of these products with the fuel forms the basis for developing predictive, physical models. One application of these models, for example, is to describe the evolution of gaseous fission products released from the fuel element to the fuel-cladding gap and plenum. The model results highlight the importance of understanding the rates of emission of fission gases when considering fuel-rod and reactor design consequences.

To ensure that readers and users of the FASTGRASS module can fully understand the fission gas model built therein, this section describes the underlying physics governing how gaseous fission products behave in irradiated nuclear fuels. The models described in the following sub-sections will lay the groundwork for understanding how these products influence fission gas release and their relationship to the evolving fuel microstructure. The sub-sections covered here deal with the concentration and distribution of gaseous fission products within the fuel, within the grain and at grain boundary, and at the so called triple-points.

There are two basic forms of fission products. The two forms, solid and gaseous, are distinguished by the gaseous product's tendency to organize itself into bubbles within the fuel. Completely soluble fission products that can replace heavy-metal atoms in the matrix and do not nucleate into bubbles are considered solid fission products [8].

The calculation of solid fission products' contribution to the description of the fuel is relatively straight forward compared to that of gaseous products. Therefore, this sub-section will concentrate on gaseous fission product behavior. Solid fission products will be discussed in another sub-section. What follows is a description of bubble behavior particular to its distribution in the matrix, e.g., within the grain or on the grain face. This will lead into a discussion of bubble interlinkage.

2.1.1 Nucleation and Growth of Intragranular Fission Gas Bubbles

The concentration of gas atoms, Cg, is determined by solving the equation,

$$\begin{aligned}\frac{dC_g}{dt} &= -16\pi F_N r_g D_g C_g^2 - 4\pi \left(D_g + D_b\right)\left(r_g + r_b\right) C_g C_b \\ &\quad - \pi \left|V_b - V_g\right| \left(r_g + r_b\right)^2 C_g C_b - S_v^{\alpha\alpha} V_g C_g + \frac{6D_g}{d_g}\frac{\partial C_g}{\partial r}\bigg|_{r=d_g/2} \\ &\quad - \frac{3C_g d_g(t) V_{gb}}{d_v^g} + \kappa \dot{f} + bN_b C_b + \delta b N_f C_f + \delta b N_e C_e \quad .\end{aligned} \tag{2.1.1}$$

In Eq. (2.1.1), r_g, r_b; D_g, D_b; and V_g, V_b are the intragranular gas atom (g) and gas bubble (b) radii, diffusion coefficients, and velocities, respectively. F_N is the bubble nucleation factor, i.e., the probability that two gas atoms that have come together will actually stick together. The term $S_v^{\alpha\alpha}$ is the grain boundary area per unit volume; d_g, the grain diameter; $\dot{f}$, the fission rate (fissions cm^{-3} s^{-1}); and κ, the number of gas atoms produced per fission.

The successive terms on the right-hand-side (RHS) of Eq. (2.1.1) represent, respectively, 1) the loss of gas atoms in dynamic solution due to bubble nucleation; the 2) random and 3) biased capture of gas atoms by bubbles; 4) biased and 5) random diffusion of gas atoms to grain boundaries; 6) loss of gas atoms due to grain-boundary sweeping; 7) gas atom generation due to fission; and 8-10) the gain of gas atoms due to gas atom re-solution from intragranular, grain face and grain edge bubbles.

The fifth term on the RHS of Eq. (2.1.1), the flux of gas atoms diffusing to the grain boundaries in a concentration gradient, is obtained by solving for the concentration of gas atoms, C_g, within a spherical grain satisfying the following equation where r is the radial coordinate on the sphere.

$$\frac{\partial C_g}{\partial t} = \frac{1}{r^2}\frac{\partial}{\partial r}\left(D_g r^2 \frac{\partial C_g}{\partial r}\right) + \kappa \dot{f} \quad , \tag{2.1.2}$$

In general, Eq. (2.1.2) is solved with the boundary conditions

$$C_g = 0 \text{ at } t = 0 \qquad \text{for } 0 \le r \le d_g/2 \quad , \tag{2.1.2a}$$

$$C_g = 0 \text{ at } r = d_g/2 \qquad \text{for } t_0 \le t \le t_0 + \Delta t \quad , \tag{2.1.2b}$$

$$\frac{\partial C_g}{\partial t} = 0 \qquad \text{at } r = 0 \text{ for } t_0 \le t \le t_0 + \Delta t \quad , \tag{2.1.2c}$$

where Δt is an increment of time.

The concentration of gas atoms in a spherical grain described in 2.1.2 is

$$\frac{1}{r^2}\frac{\mathrm{d}}{\mathrm{d}r}\left(D_g r^2 \frac{\mathrm{d}C_g}{\mathrm{d}r}\right) - \frac{C_g}{\delta t} + \frac{C_g^0}{\delta t} + \kappa \dot{f} = 0 \quad . \tag{2.1.3}$$

Euler's theorem may now be used to obtain a variational principle equivalent to Eq. (2.1.3):

$$\delta \int_0^{1/2d_g} 4\pi \left[\frac{D_g}{2}\left(\frac{\mathrm{d}C_g}{\mathrm{d}r}\right)^2 + \frac{C_g^2}{2\delta t} - \left(\frac{C_g^0}{\delta t} + \kappa \dot{f}\right) C_g\right] r^2 \mathrm{d}r = 0 \quad , \tag{2.1.4}$$

which assumes that Dirichlet boundary conditions are to be applied. An approximate solution to the problem may now be obtained by choosing a trial function that satisfies the boundary conditions and minimizes the integral in Eq. (2.1.4) in terms of free parameters in the function. Many types of trial functions could be chosen, but piecewise functions are easier to handle than global functions. Quadratic functions are attractive because they allow an exact representation of Eq. (2.1.2) for long times. To provide a reasonable degree of accuracy with a minimum calculation time, the spherical grain is split into two concentric regions of approximately equal volume, shown in Fig. 1. In each region, the gas concentration is represented by a quadratic function constrained to have $dC_g/dr = 0$ at $r = 0$. In Fig. 1, outer Region II, the concentration function is constrained to a value of $C_g = 0$ at $r = d_g/2$. The two functions are also constrained to be continuous at the common boundary of the two regions. This leaves three free parameters. Mathews and Wood [9] chose these to be the concentrations C_g^1, C_g^2 and C_g^3, respectively, for the radius ratios $\rho_1 = 0.4$, $\rho_2 = 0.8$, and $\rho_3 = 0.9$, where $\rho = 2r/d_g$. These positions are the midpoint radius of Region I, the boundary between the regions, and the midpoint radius of Region II, respectively.

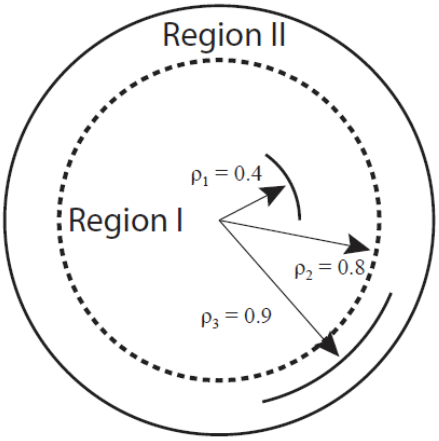

Figure 1: Configuration of the two zone model

Thus the trial functions are as follows:

For Region I,

$$C_g = C_1^g \left(0.64 - \rho^2\right) /0.48 + \left(\rho^2 - 0.16\right) /0.48 \quad . \tag{2.1.4a}$$

For Region II,

$$C_g = 5C_2^g \left(10\rho^2 - 19\rho + 9\right) + 10C_3^g \left(18\rho - 10\rho^2 - 8\right) \quad . \tag{2.1.4b}$$

Eqs. (2.1.4a) and (2.1.4b) are substituted for Cg in Eq. (2.1.4) and an extremum is found by differentiating with respect to C_g^1, C_g^2 and C_g^3 in turn. The following three linear equations are thus obtained:

$$\left(q_1 D_g/d_g^2 + q_2/\delta t\right) C_1^g + \left(q_3 D_g/d_g^2 + q_4/\delta t\right) C_2^g = K_g q_5 + \left(C_1^0 q_2 + C_2^0 q_4\right) /\delta t \quad , \tag{2.1.4c}$$

$$\left(q_3 D_g/d_g^2 + q_4/\delta t\right) C_1^g + \left(q_2 D_g/d_g^2 + q_7/\delta t\right) C_2^g + \left(q_8 D_g/d_g^2 + q_9/\delta t\right) C_3^g = K_g q_{10} + \left(C_1^0 q_4 + C_2^0 q_7 + C_3^0 q_9\right) /\delta t \quad , \tag{2.1.4d}$$

$$\left(q_9 D_g/d_g^2 + q_9/\delta t\right) C_2^g + \left(q_{11} D_g/d_g^2 + q_{12}/\delta t\right) C_3^g = K_g q_{13} + \left(C_2^0 q_9 + C_3^0 q_{12}\right) /\delta t \quad , \tag{2.1.4e}$$

where C^0_1 , C^0_2 and C^0_3 are the values of the concentrations at the evaluation points at the start of the time increment. The various q coefficients are integrals, which, when directly evaluated, are, to four significant figures

$q_1 = 4.552$, $q_2 = 0.06935$, $q_3 = -4.552$,

$q_4 = 0.02167$, $q_5 = 0.09102$, $q_6 = 37.78$,

$q_7 = 0.07614$, $q_8 = -38.72$, $q_9 = 0.008456$,

$q_{10} = 87.04$, $q_{11} = 0.08656$, $q_{12} = 0.01008$,

$q_{13} = 0.1083$.

Equations (2.1.4c) - (2.1.4e) can be directly solved to obtain the concentrations C_1, C_2 and C_3 as follows:

$$C_1^g = \frac{X_1 - F_2 C_2^g}{F_1} \quad , \tag{2.1.4f}$$

$$C_2^g = \frac{\frac{F_2}{F_1} X_1 + \frac{F_4}{F_5} X_3 - X_2}{\frac{F_2}{F_1} F_2 + \frac{F_4}{F_5} F_4 - F_3} \quad , \tag{2.1.4g}$$

and

$$C_3^g = \frac{X_3 - F_5 C_2^g}{F_5} \quad , \tag{2.1.4h}$$

where

$$F_1 = q_1 D_g / d_g^2 + q_2 / \delta t, \qquad F_2 = q_3 D_g / d_g^2 + q_4 / \delta t,$$

$$X_1 = K_g q_s + \left(C_1 q_2 + C_2 q_4\right) / \delta t,$$

$$F_3 = q_5 D_g / d_g^2 + q_6 / \delta t, \qquad F_4 = q_7 D_g / d_g^2 + q_8 / \delta t,$$

$$X_2 = K_g q_{10} + \left(C_1^0 q_4 + C_2^0 q_6 + C_3^0 q_8\right) / \delta t,$$

$$F_5 = q_9 D_g / d_g^2 + q_{10} / \delta t, \text{ and}$$

$$X_3 = K_g q_{13} + \left(C_2^0 q_8 + C_3^0 q_{10}\right) / \delta t \quad .$$

The flux of gas atoms to the boundary (in units of atoms · cm^{-3} · s^{-1}) is given by

$$J = \frac{6 D_g}{d_g} \frac{\partial C}{\partial r}\bigg|_{r = d_g/2} \quad , \tag{2.1.4i}$$

$$J = \frac{D_g}{d_g^2} \left(-60 C_2^g + 240 C_3^g\right) \quad . \tag{2.1.4j}$$

To couple the diffusive flow process to other processes that affect fission gas behavior, (e.g., gas atom re-solution, gas atom trapping by bubbles, and gas bubble nucleation and coalescence), the average concentration of fission gas within the grain is needed.

Matthews and Woods [9] determined that the best expression for the average fission gas concentration within the grain, C_g, is given by

$$\overline{C}_g = 0.2876C_1^g + 0.2176C_2^g + 0.4216C_3^g \quad . \tag{2.1.4k}$$

At the end of the iteration, the concentrations C1, C2, and C3 in Eq. (2.1.4k) are scaled by imposing the condition that the average concentration calculated by use of Eq. (2.1.4k) is equal to the average concentration calculated by use of Eq. (2.1.1), i.e., that

$$\overline{C}_g = C \quad . \tag{2.1.4l}$$

The modified $C^g{}_1$, $C^g{}_2$, and $C^g{}_3$ then become the initial values of these concentrations (i.e., $C^0{}_1$, $C^0{}_2$, and $C^0{}_3$) to be used in the next iteration. The diffusive flow of fission-gas bubbles is treated in a manner analogous to that for the fission-gas atoms, but with $\dot{f} = 0$ in Eq. (2.1.2). This method of coupling diffusive flow to other processes that affect fission-gas behavior is computationally efficient and has been benchmarked against various analytical solutions [9].

The last three terms on the RHS of Eq. (2.1.1) account for the effects of fission-induced gas atom re-solution depending on the rate, b, at which gas atoms are ejected from the bubble. The rate b is calculated under the assumption that gas atom re-solution from a spherical bubble is isotropic and proceeds by the knocking out of single gas atoms. Thus,

$$b = \frac{3b_0\dot{f}}{r_b^3} \int_{r_b-\lambda}^{r_b} \left(\frac{1+\cos\theta}{2}\right) r^2 \mathrm{d}r \quad , \tag{2.1.5}$$

A straightforward integration of Eq. (2.1.5) results in

$$b = \frac{3b_0\dot{f}}{r_b^3}\left(G_2 - G_1\right) \quad , \tag{2.1.5a}$$

where

$$G_2 = r_b^2\left[\frac{r_b}{6} + \frac{r_b^2}{16\lambda} + \frac{1}{8}\left(\lambda - \frac{r_b}{\lambda}\right)\right] \quad , \tag{2.1.5b}$$

$$G_1 = (r_b-\lambda)^2\left[\frac{r_b-\lambda}{6} + \frac{(r_b-\lambda)^2}{16\lambda} + \frac{1}{8}\left(\lambda - \frac{r_b}{\lambda}\right)\right] \quad , \tag{2.1.5c}$$

where λ is the average distance an ejected atom travels and b_0 is a measurable property of the material.

The last two terms of Eq. (2.1.1) contain the variable δ, which is a measure of the "strength" of gas atom re-solution from grain boundary bubbles. The magnitude of δ is closely related to what is formally known as backward flux [10].

To solve for C_g with Eq. (2.1.1), a number of terms on the RHS must be determined. RHS Terms 2, 3, 6 and 8 depend on C_b. The equation for C_b, the concentration of intragranular bubbles, is given by

$$\frac{\mathrm{d}C_b}{\mathrm{d}t} = -16\pi F_N r_g D_g C_g^2/N_b + 4\pi\left(D_g + D_b\right)\left(r_g + r_b\right) C_g C_b/N_b$$
$$+ \pi\left|V_b - V_g\right|\left(r_g + r_b\right)^2 C_g C_b/N_b - S_v^{\alpha\alpha} V_b C_b + \frac{6D_g}{dg}\frac{\partial C_b}{\partial r}\Big|_{r=d_g/2} \quad (2.1.6)$$
$$- \frac{3C_b}{d_g} V_{gb} - bC_b + \frac{3V_{gb}}{d_g} N_b \left(\frac{K_f}{N_f} C_f + \frac{K_e}{N_e} C_3\right) \quad .$$

The origins of the first six terms on the RHS of Eq. (2.1.6) are analogous to those given for Eq. (2.1.1). The last term accounts for the introduction of grain face and grain edge bubbles into the lattice due to bubble pull-off from a moving grain boundary, and/or the presence of large temperature gradients. If the bubbles are bigger than a given critical size, K_f and/or $K_e = 1$; otherwise K_f and $K_e = 0$.

2.1.2 Intergranular Fission Gas: Grain Faces and Edges

Six basic quantities must be determined before Eqs. (2.1.1) and (2.1.6) can be solved. V_{gb} is the velocity of the moving grain boundary. C_f, C_e are discussed in this section. The section following describes how N_b, N_f, and N_e are calculated.

The equation for C_f, the concentration of gas bubbles on the grain faces (assuming the grains have an approximate tetrakaidecahedral structure), is given by

$$\frac{\mathrm{d}C_f}{\mathrm{d}t} = -\delta b C_f - \frac{3V_{gb}}{d_g} K_f C_f - \varkappa V_f C_f - \frac{V_f \Phi_\chi}{d_g C_f} - \frac{P_A C_f}{t}$$
$$+ S_v^{\alpha\alpha}\left(\frac{V_g C_g}{N_f} + \frac{V_b C_b N_b}{N_f}\right) - \frac{6}{d_g}\left[\frac{D_g}{N_f}\frac{\partial C_g}{\partial r}\Big|_{R=d_g/2} + \frac{D_b N_b}{N_f}\frac{\partial C_b}{\partial r}\Big|_{R=d_g/2}\right]$$
$$+ 3d(t) V_{gb}\left(\frac{C_g}{N_f} + \frac{C_b N_b}{N_f}\right)/d_g \quad . \qquad (2.1.7)$$

The first and second terms on the RHS of Eq. (2.1.7) are loss terms due to bubble destruction by gas atom re-solution and bubble pull-off, respectively. The third term represents the loss of grain-face bubbles due to biased migration out of the node, where V_f is the velocity of a bubble on the grain face and $\varkappa$ = cross-sectional area of the node boundary/volume on the node; a node in a solid fuel generally has the shape of a cylindrical annulus. The fourth and fifth terms represent the biased grain-face bubble migration and migration of grain-face gas through grain-face channels to the grain edges. Φ_χ is the average number of grain faces per grain. Similar to the terms found in Eq. (2.1.1), the last three terms represent the biased diffusion of fission-gas atoms and bubbles from the lattice, the random diffusion of fission-gas atoms and bubbles from the lattice, and the gain of fission-gas atoms and bubbles by the grain-boundary sweeping mechanism, respectively.

The equation for C_e, the grain edge bubble concentration, is given by

$$\frac{\mathrm{d}C_e}{\mathrm{d}t} = -\delta b C_e - \frac{3V_{gb} K_e C_e}{d_g} + V_f \frac{\Phi_\chi}{d_g}\frac{N_e}{N_f}\left(1 - P_I\right) C_f$$
$$+ P_A \frac{N_e}{N_f}\left(1 - P_I\right)\frac{C_f}{t} - \frac{\mathrm{d}P_I}{\mathrm{d}t} C_e \quad . \qquad (2.1.8)$$

In Eq. (2.1.8), the last term on the RHS represents gas lost through long-range interconnection of grain edge porosity to a free surface. The FASTGRASS model for calculating the probability of long-range grain interconnection is based on the assumption that the long-range interconnection is a function of the

swelling of grain-edge bubbles. This assumption is supported by experiment [11] as well as theory [12]. To account for the local fluctuations in fuel microstructure and gas bubble morphology, the grain-edge/porosity interlinkage fraction, P_I, is assumed to be a statistical distribution around an average value of the grain-edge swelling, B_{vedge}:

$$P_I = \frac{1}{\sigma_e \sqrt{2\pi}} \int_{x=B_{crit}} exp\left[\frac{-(x - B_{vedge} - B_{vpor})^2}{2\sigma_e^2}\right] \mathrm{d}x \quad , \tag{2.1.9}$$

where $B_{vedge} = 4/3\pi R_e 3\sigma_e C_e$, and σ_e is a geometrical factor that accounts for the ellipsoidal shape of grain-edge bubbles. $B_{crit} = 0.05$ is the value of grain edge swelling at which long-range interconnection would take place if the fuel microstructure and gas bubble morphology were homogeneous; $B_{vpor} = 0.0$ for $\rho >= 92\%$ of the theoretical density. In the absence of microcracking, the fission gas that would have been vented via the cracks remains on the grain boundaries. Note that FASTGRASS contains a model for intergranular microcracking due to overpressurized fission-gas bubbles, discussed in [11]. The effects of microcracking on interlinkage are included by redefining P_I as $P_I = \max(P_I, Mc)$, where Mc is the fraction of grain-boundary area/volume which has opened up due to microcracking. Retained grain-edge fission gas causes deformation of the grain edges (i.e., grain-edge fission-gas-bubble swelling), and the subsequent increase in long-range interconnections of grain edge tunnels. This interconnection of grain-edge tunnels provides the pathways for enhanced fission-gas release.

Gas atoms that are knocked out of grain boundary bubbles are evenly dispersed within an annulus of thickness λ adjacent to the grain boundary. This backward flux of gas atoms affects the concentration gradient of gas atoms from the matrix to the boundary, and thus the overall flux of gas atoms to the boundary. Therefore, this backward flux of gas atoms, in atoms $\cdot$ m^{-2} $\cdot$ s^{-1}, can be thought of as an additional matrix gas-atom generation mechanism and is given by

$$\dot{f}(\lambda)_{boundary} = \frac{3bN_b n(t)}{d_g} \frac{V}{V_\lambda} \quad , \tag{2.1.10}$$

where V is the volume of the grain and V_λ is the volume of the annulus of thickness λ within which the backward flux of gas atoms from the boundary bubbles is deposited. The term n(t) is the number of gas atoms in a grain boundary bubble, given by

$$n(t) = \sum_{\delta t} \left(\frac{f_c J(t)}{N_b} + z\,(1 - f_c)\, D_g C_g^b - bn(t) \right) \delta t \quad , \tag{2.1.11}$$

where b is the gas-atom re-solution rate, $fc = \pi R_b N_b$ is the fractional coverage of the grain boundary by bubbles, z is the grain-boundary diffusion enhancement factor, N_b is the total number of bubbles on the boundary (in bubbles $\cdot$ m^{-2}), and C^b_g is the gas-atom concentration on grain boundaries (in atoms $\cdot$ m^{-2}). C^b_g is given by

$$C_g^b = \sum_{\delta t} \left((1 - f_c)\, J(t) + z D_g C_g^b N_b \right) \delta t \quad . \tag{2.1.12}$$

When fc is small (e.g., during the initial stages of boundary-bubble growth), most of the gas reaching the boundary exists as single gas atoms and diffuses by random walk to the boundary bubbles. This is analogous to gas atom accumulation by bubbles in the grain interior. When f_c is large, the majority of the gas reaching the boundary flows directly into boundary bubbles. The grain boundary enhancement factor, z, accounts for the general view that gas atom diffusion on the boundary is more rapid than in the matrix due to the existence of more space and sites (e.g., ledges) from which and to which the gas atoms can hop.

In Eq. (2.1.10), the first ratio on the right hand side represents the backward flux of gas (atoms · m^{-2} · s^{-1}) and the second ratio the fraction of the intragranular volume within which this gas is deposited. This value is independent of λ. Therefore as λ decreases, V_λ becomes smaller and $\dot{f}(\lambda)$boundary increases.

Equations (2.1.1), (2.1.6), (2.1.7), and (2.1.8) express mass balance and are solved by assuming that the average number of atoms per bubble does not change over the integration time step, i.e., $N_b = N_f = N_e = 0$. Subsequent to the calculation of the C_is, changes in N_i are calculated by examining the bubble growth and shrinkage fluxes that influence the average size bubble. For example, changes in N_b are calculated by evaluating

$$\begin{aligned}\dot{N}_b \propto & \frac{1}{C_b}\left[16\pi r_b D_b C_b^2 + \pi r_b^2 \alpha_b V_b C_b^2\right. \\ & + 4\pi\left(D_g + D_b\right)\left(r_g + r_b\right)\frac{C_g C_b}{N_b} - bC_b \\ & \left. -16\pi F_N r_g D_g C_g^2 + \frac{3V_{gb}N_b}{d_g}\left(\frac{K_f}{N_f}C_f + \frac{K_e}{N_e}C_e\right)\right] \quad . \end{aligned} \tag{2.1.13}$$

In Eq. (2.1.13), the first three terms on the RHS correspond to the growth of the average size bubble due to random and biased coalescence of these bubbles with each other, and the growth of these bubbles due to accumulation of gas atoms. The 4th and 5th terms on the RHS of (2.1.13) represent the shrinkage of the average size bubble due to bubble destruction by fission-induced gas atom re-solution, and due to the generation of very small bubbles by gas atom nucleation (the introduction of small bubbles will tend to bias the average size bubble toward smaller sizes). The last two terms represent the growth of the average size bubble by introducing into the lattice larger grain face and grain-edge bubbles which have become detached from the moving grain boundary. The proportionality sign in (2.1.13) indicates that the changes in N_b are computed using a numerical algorithm which evaluates (2.1.13) and increments or decrements N_b by an amount proportional to this value. When N_b is calculated in this fashion, it agrees very well with results of calculations for the evolution of the bubble size distribution made with the GRASS-SST mechanistic model [5]. The equations for $\dot{N}_f$ and $\dot{N}_e$ are analogous to Eq. (2.1.13).

2.1.3 Bubble Interlinkage

Fission gas can migrate from the grain faces to the grain edges by (random or biased) diffusion via short circuit paths created by grain-face channel formation (i.e., interlinkage of grain-face bubbles). The grain-face channel formation is a function of the amount of gas on the grain faces. Calculation of grain face saturation by fission gas in FASTGRASS is done by directly addressing the calculated distribution of fission-gas bubble sizes. The projected areal coverage of the grain face by these bubbles, per unit volume, is given by

$$A_F = \pi R_f^2 C_f f_f(\theta) \quad , \tag{2.1.14}$$

where R_f is the average radius of grain-face bubbles and $f_f(\theta)$ is a geometrical factor that accounts for the lenticular shape of the these bubbles. If the gas is assumed to be made up of equal, closely packed, touching bubbles, the maximum areal coverage per unit area of grain-face is $A^*_F = 0.907$. Note that under conditions where this assumption is not valid ($A^*_F < 0.907$), the FASTGRASS code utilizes a nominal value of $A^*_F = 0.50$. Grain-face saturation (i.e., the initiation of gas channel formation) occurs when

$$A_F \geq A_F^* S_v^{\alpha\alpha} \quad , \tag{2.1.15}$$

where $S_v^{\alpha\alpha}$ is the grain-face area per unit volume.

Equations (2.1.14) and (2.1.15) do not account for local variations in fuel microstructure. To include these effects in the calculations of grain-face channel formation, it is assumed that the local variations in fuel microstructure can be represented by the width (σ_f) of a distribution of A (given by Eq. (2.1.14)) such that the fraction of grain-face channel interlinkage is given by

$$P_A = \frac{1}{\sigma_f \sqrt{2\pi}} \int_{x=A_F^* S_v^{\alpha\alpha}} exp\left[\frac{(-x-A)^2}{2\sigma_f^2}\right] \mathrm{d}x \quad . \tag{2.1.16}$$

The width of the distribution in Eq. (2.1.16) is a function of erratic structural parameters, depending on local fuel condition and heterogeneity; in principle, it can be determined experimentally.

Larger grains have a smaller grain-face area per unit volume, so for a given distribution of fission gas, the grain faces of larger grains reach their saturation limit quicker than those of small grains (see Eq. (2.1.16)), and thus vent their fission gas content to the grain edges sooner. At higher temperatures, increased coalescence rates lead to larger bubbles on the faces; these larger bubbles link up more easily to vent gas to the grain edges. Therefore, a combination of high temperatures and large grain size results in more rapid and extensive channel formation, and hence, in quicker gas transport from the grain faces to the edges.

2.1.4 Fission Gas Release

Nuclear reactor design requires a sound understanding of fission gas release from the irradiated nuclear fuel. Determination of fission gas release not only takes into account gas released into the fuel–cladding gap, but also gas that travels to the central void and open porosity sites (e.g., cracks and interlinked gas bubbles) within the fuel [8]. Gaseous fission products can be grouped into two major categories consisting of the noble gases xenon (Xe) and krypton (Kr) (although Xe is generated in much larger proportions than Kr) and volatile fission products (VFP) such as cesium (Cs), iodine (I), tellurium (Te), barium (Ba) and strontium (Sr).

The mechanism for fission gas release has been covered throughout the present work. The mechanisms that drive the release of fission gases are similar to those responsible for swelling. Generally, the swelling process continues until grain boundary bubbles interlink on the grain faces leading to short-circuit paths for gas atom venting to the grain edge. At the grain edge, extensive bubble interlinkage can form long tunnels that channel fission gases to the surface or other free volumes in the fuel. In FASTGRASS, the model for calculating the probability of long-range grain-edge bubble interconnection is a function of grain-edge bubble swelling. To account for local fluctuations in fuel microstructure and gas-bubble morphology, the grain-edge-porosity interlinkage fraction, F, is assumed to be a statistical distribution around an average value of the grain-edge swelling, B_{vedge}, given by Eq. (2.1.9).

At low temperatures ($<< 0.5T_m$), gas atom diffusion is athermal and mobility is minimal making migration to the surface or porosity unlikely. In this regime, most of the vented gas occurs close to the surface as a result of recoil or fission fragment knockout [8]. Gas release by either of these processes is nominal. High temperature gas release can be divided into two primary temperature ranges. At temperatures between 1300 and ~1900K in UO_2, for example, gas release is determined by thermal diffusion of gas atoms to the surface and although the temperature gradient is generally not strong enough for gas bubbles to move, long-range bubble interlinkage may occur and provide another venting channel. When temperatures increase above 1900K, gas bubbles and closed pores can move through the fuel along the temperature gradient and vent directly to the surface or other free volume spaces [8].

The total contribution to fission gas release, g, is calculated in FASTGRASS by the following expression:

$$\frac{\mathrm{d}g}{\mathrm{d}t} = \left(\frac{V_f \sqrt{14}}{d_g} C_f + \frac{P_A C_f}{t} \right) P_I + C_e \frac{\mathrm{d}P_I}{\mathrm{d}t} + V_f \varkappa C_f \quad . \qquad (2.1.17)$$

For a multinode calculation, the various gas release contributions from each individual node, given by Eq. (2.1.17), are summed to obtain the total gas released during time t. The total contribution of gas released due to long-range migration of fission gas bubbles up the temperature gradient depends on the cross-sectional area of the inner or outer node based on the direction of the gradient which bounds a free surface. The velocity of the grain-face bubbles is given by V_f.

2.2 FASTGRASS Code Modification and Implementation

This sub-section describes the necessary modifications to the FASTGRASS code and the details of its implementation in the BISON code.

2.2.1 Structure and Data Flow of the FASTGRASS code

The Fortran FASTGRASS code consists of a number of subroutines that handle initialization, input/output (I/O), calculation of various key variables (e.g., diffusion coefficient of gas and irradiation enhanced diffusivity), solving fission gas equation of state, and, most importantly, solving the five main differential equations by iteration.

In this sub-section, the functionalities of these subroutines are presented in detail to clarify the code structure and data flow of the FASTGRASS code and thereby the corresponding module implemented in the BISON code framework.

Fig. 2 shows a schematic flow diagram of the FASTGRASS code in its standalone operation form. The main function of the code, *fastgrass*, performs simple I/O functionalities: setting up the problem with user provided input parameters. In the FASTGRASS module implemented in the BISON code, this function, as a subroutine, handles communications between the module and the BISON main framework by receiving state variables calculated and processed in the BISON code. The subroutine *zrdwr* manages the initialization at the beginning of each FASTGRASS time step and the preparation of the next time step. The counterpart subroutine in the BISON code also prepares FASTGRASS variables for the next BISON time step. To this end, more functionality was added to the subroutine when implementing it in the BISON code. The importance of the added functionality will be described in the next section, where details of the implementation of the FASTGRASS module are presented.

Once initialization is complete, the subroutine *grassf* is called. This subroutine is the main framework of the code, directing the simulation to each subroutine and summarizing the results for output purposes at the end of each output time step. Subroutine *grs1*, which calculates and updates key state variables such as diffusivities and resolution rates, and subroutine *grs2*, which solves the main differential equations, are called from *grassf* in an iterative manner. Other subroutines perform more specific functions of the simulation. Subroutine *ronk* calculates parameters for a hard sphere approximation of the fission gas equation of state. It is called when the average bubble radius is below 0.25 μm. Subroutine *frclc* handles the fission gas equation of state calculations. Subroutine *rdcal* together with subroutine *hybr* iteratively update average gas bubble size. There is a numerical algorithm implemented in *rdcal* that ensures a quick convergence of average bubble size. As can be expected, subroutine *rdcal* also interacts with subroutines *grs1* and *grs2* through *grassf* in an iterative manner to solve for the average bubble sizes and bubble number densities inside the grain, on grain faces, and grain edges, respectively. In addition, subroutines *hyb* and *fconc* together handle the calculation of chemical

equilibria, determining the distribution of chemical constituents, i.e., the uranium, oxygen, and fission products in the oxide version of the code.

After each time step, whose length is calculated in *grassf* based on convergence, subroutine *grassf* redirects the simulation to subroutine *zrdwr* to prepare variables for the next time step. When the user-specified total simulation time is reached, the program will end after the final printout of output quantities by subroutine *grassf*.

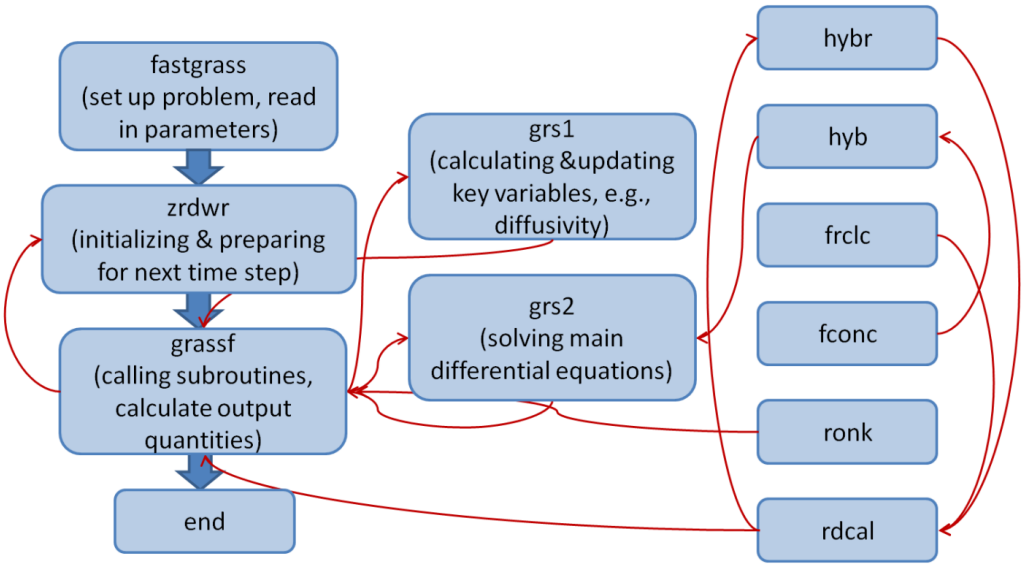

Figure 2: Schematic flow diagram of FASTGRASS code

2.2.2 Discretization of Geometry by the FASTGRASS code

The rendering of a computational geometry in FASTGRASS is very similar to that in other early-developed fuel performance codes, e.g., LIFE-METAL. It is essentially a 2-D axisymmetric representation of the fuel pellet. The original Fortran 77 version of the FASTGRASS code allows only 10 axial and radial nodes, mainly due to the limited computational power at the time the code was initially developed. The code in its current form has relaxed these limitations by expanding the size of the arrays considerably. This is potentially memory consuming, but not to the extent that it will strongly impact the simulation time unless a very fine nodal discretization is needed.

It should be pointed out that the state variables (except temperatures) of each node are represented by values in the geometric center of that node. Temperatures are defined in the FASTGRASS code on the boundaries in the radial directions, i.e., the inner and outer surfaces of each nodal ring. Axially, they are still defined in the center of the corresponding nodes. In our initial attempt to implement FASTGRASS in the BISON code, we tried to make the geometry discretization by FASTGRASS compatible with the BISON meshing mechanism. However, the BISON code requires more advanced ways of meshing fuel pellet geometry, including compatibility with different mesh element geometries and compatibility with 3-D meshing. Consequently, we have taken another route by modifying the FASTGRASS code to make it possible to execute the FASTGRASS module when each single element is called upon by the BISON code.

2.2.3 C++ Version of the FASTGRASS Module

We started efforts to implement the FASTGRASS model into the BISON code by translating the FASTGRASS code from its original Fortran 77 form to a standalone operational C++ counterpart.

This standalone fission gas behaviors code in its C++ programming language form was constructed by putting together all essential subroutines and then debugging and testing. A thorough step-by-step verification was performed to ensure that the C++ code produces exactly the same results as the original FASTGRASS code at each time step given the same input parameters.

To demonstrate the validity of the C++ version of the FASTGRASS code and thereby to verify the functionality of the subroutines implemented in the BISON code, a simple single node simulation was performed with both the original Fortran version of the code and the newly built C++ version. Single node verification was performed because the FASTGRASS module utilized in the current implementation of the BISON code uses only single node (mesh element) calculation.

Fig. 3 compares the fractional fission gas release results generated by both code simulations. In this comparison, both a simple case with zero hydrostatic stress and a case with 10 MPa fixed hydrostatic stress were used. The intent was to clarify the consistency on both temperature and hydrostatic stress bases.

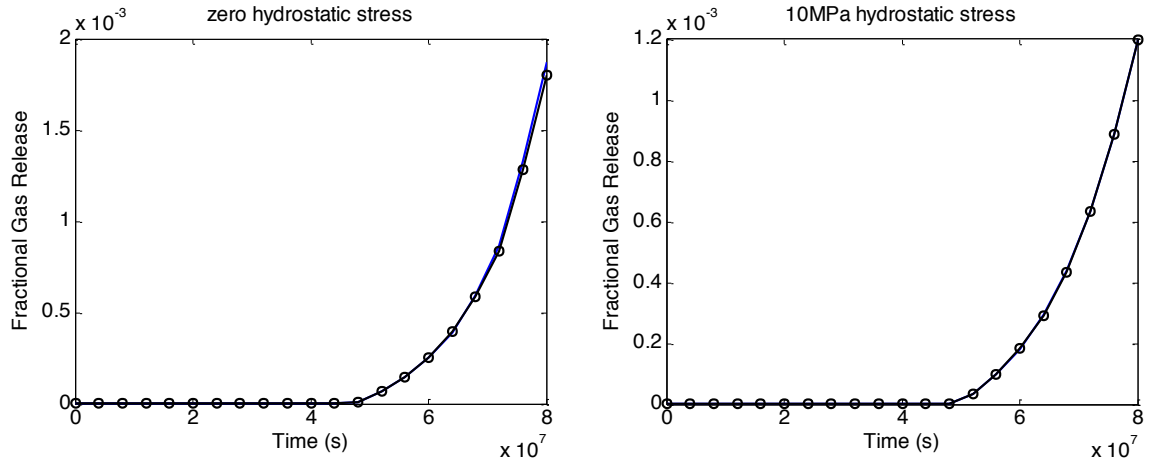

Figure 3: Comparison of single node fractional gas release between the Fortran FASTGRASS code and the C++ FASTGRASS code: (a) with zero hydrostatic stress and (b) with 10 MPa fixed hydrostatic stress.

It can be clearly observed that both codes produce the same results. In fact, the results only differ beyond three significant digits. These small differences could be a result of Fortran 77 and C++ handling numerical operations at slightly different precision levels. With the large number of iterations involved in the simulations, a small such difference is possible.

2.2.4 Implementation of the FASTGRASS Model into the BISON Code

Implementation of the FASTGRASS fission gas model as a module into the BISON code requires very good familiarity with the BISON code data structure. With the FASTGRASS module in C++ code form, an internal incorporation was eventually realized.

One of the challenge in coupling the fission gas model and the BISON code was resolving the time stepping algorithm. As the fission gas behaviors model has its own scheme of determining appropriate time steps that is independent from BISON time steps, the coupling needs to first provide a mechanism to run the fission gas model following the BISON time stepping scheme. This was done by setting the

initial trial time step in FASTGRASS to a small fraction of the BISON time step and then using regression-based methods to extrapolate key state variables used by the fission gas model in its own time grid in between two given BISON time steps to inform the FASTGRASS model.

For each mesh element, an approximate average temperature is derived by averaging the temperatures at each node. Similarly, the average hydrostatic stress is derived by averaging the hydrostatic stresses at each node of the element.

For the purpose of demonstrating successful coupling of the fission gas model with the BISON code, a coarse mesh with smeared geometry model of BISON was taken. A simulation run of the FASTGRASS module was performed for each mesh element of BISON separately. This is the way the BISON code was originally structured to perform fission gas simulations - with its subroutines built in the source file ForMas.C, where the Forsberg-Massih model is utilized to model fission gas release [13].

2.2.5 Demonstration

To demonstrate successful implementation of the FASTGRASS model into the BISON code, it is necessary to compare a simple BISON simulation following FASTGRASS module implementation to a standalone FASTGRASS simulation.

Fig. 4 shows the simulated fractional fission gas release calculated by the BISON code with the FASTGRASS module (the blue curve) together with that calculated by the FASTGRASS standalone code (red curve). The simulation case used here is an example problem in the BISON repository at the Idaho National Laboratory. This simple simulation case is used to demonstrate the current implementation of the FASTGRASS module.

It should be noted that the change in state variables such as temperature and hydrostatic stress were calculated from the BISON code and passed to the FASTGRASS standalone code as input parameters. A coarse spatial and temporal discretization was used for the FASTGRASS standalone simulation. It was also observed that the values of the total fission gas generated by these calculations are consistent as they are a pure reflection of the power density (or fission density) and the yield of fission gas species.

It is necessary to point out that some approximations (namely, ignoring radial and axial long range transport of fission gas between different mesh elements) have been made in the current implementation of the FASTGRASS module into the BISON code. Consequently, the difference between the BISON calculated fractional fission gas release and that calculated by the FASTGRASS standalone code reflects, to some extent, the effect of long range fission gas transport between mesh elements.

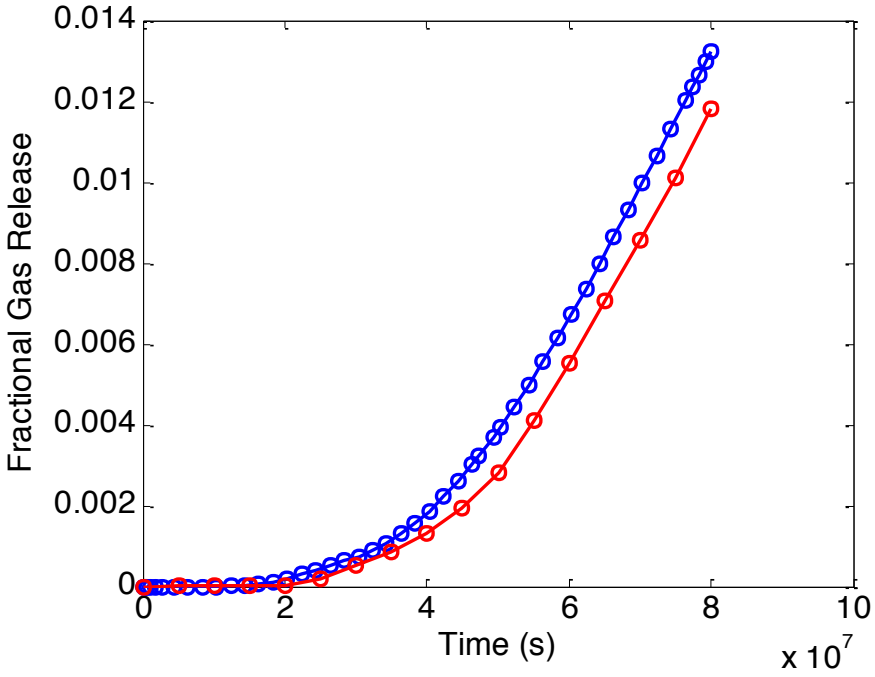

Figure 4: Comparison between fractional fission gas release calculated by the BISON code with the FASTGRASS module (the blue curve) and that calculated by the FASTGRASS standalone code (red curve).

3. Ion Implantation on Large-grained UO_2

The meso-scale nature of MARMOT makes it difficult to rely directly on existing engineering data to benchmark and validate its physics models. Specifically designed separate effect experiments, however, can be of great assistance. To validate the Fission Gas Release Model in MARMOT, in-pile radiated UO_2 samples with different burnup levels are ideal for studying the gas. However, the extremely high radioactivity of these samples makes handling and PIE work difficult. More importantly, multiple factors contribute to the behavior and characteristics of in-pile radiated fuel (e.g., the solid fission products and high thermal gradients within pellets). To isolate a single factor from the complex multi-factor nature of in-pile fuel is very difficult. Therefore, in order to produce more "clean" samples with only fission gas, we implanted Xe gas, a primary fission gas in nuclear fuel, into UO_2 samples. The implantation followed by future post-irradiation annealing will produce the needed single-effect scenario in the fuel, where no solid fission products or other complex in-pile irradiation effects are involved.

3.1 Irradiation Chamber Building

Irradiation experiments were conducted in a high-vacuum environment with controlled temperature at ATLAS at ANL. Fig. 5 shows the irradiation chamber recently built specifically for the irradiation experiment. With gate valves connected to the inlet and outlet of the irradiation chamber, the chamber can be isolated and thus avoid possible contamination of the components up- and down-stream in the ATLAS beamline when venting to load and unload samples.

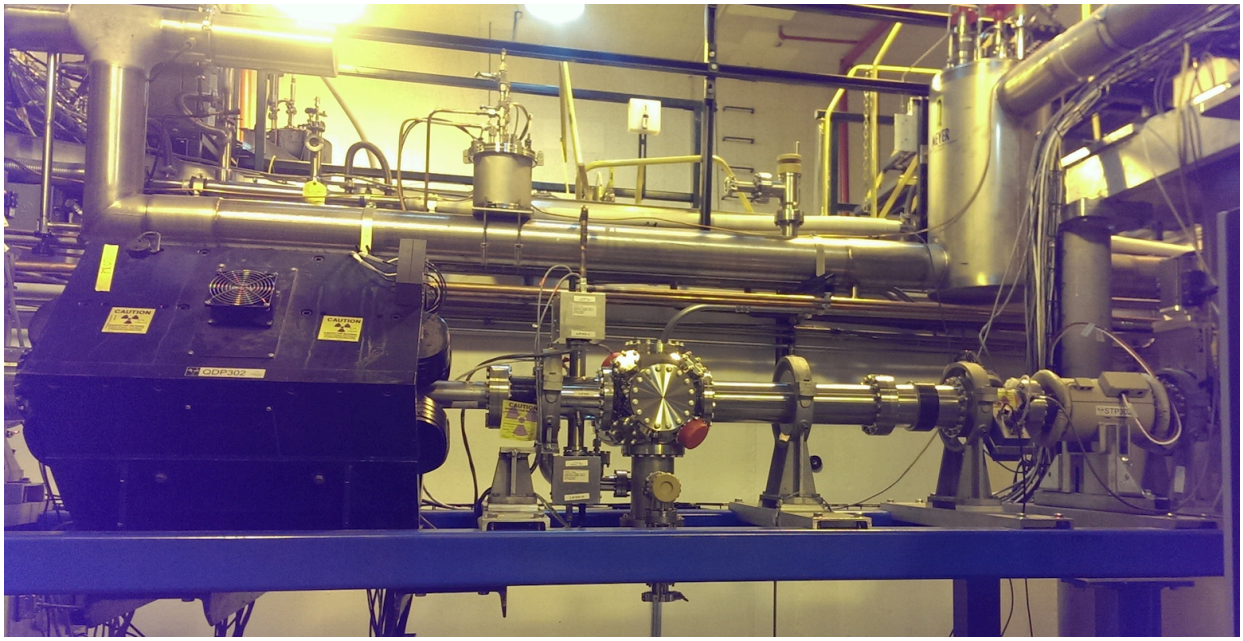

Figure 5: Irradiation chamber in the ATLAS

To provide accurate ion current reading and real–time monitoring of the sample temperature, a vacuum chamber with multiple ports is needed to allow a number of instrumentation connections. Fig. 6 shows the design of the sample stage. All wires, including thermocouple wires (for temperature measurements) and electrical wires (for ion current measurements), are connected to the sample stage through a six-way feed-through flange at the top. To provide another temperature measurement, in addition to the values given by thermocouples that connected to the back of the samples, an infrared (IR) camera (FLIR E50) was used to provide a temperature measurement of the sample surface. Fig. 7 shows the scheme of the infrared camera measurement, and an example of infrared imaging of temperature measurement.

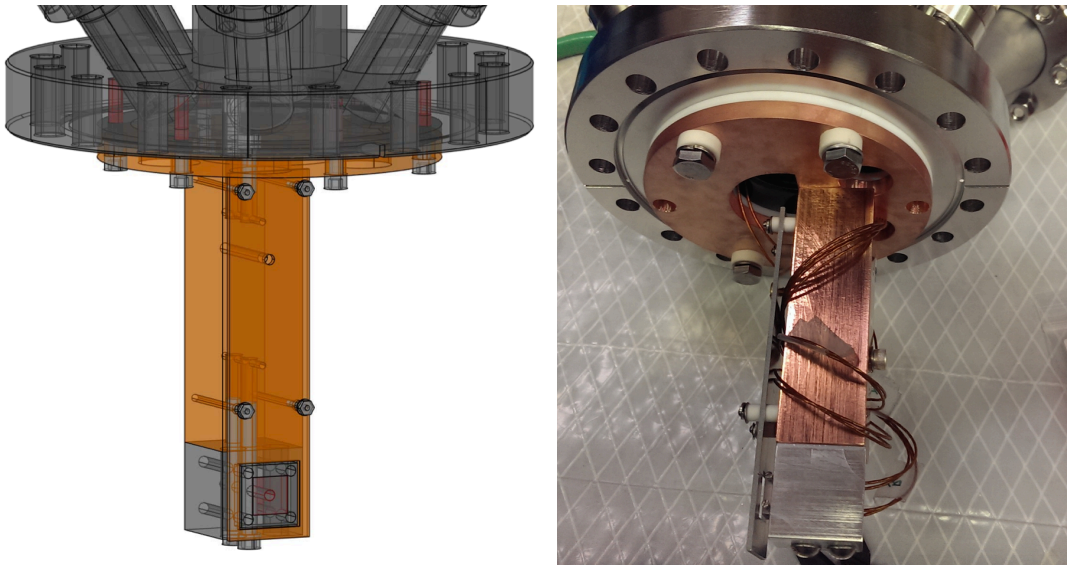

(a) (b)

Figure 6: Sample stage for ATLAS irradiation: (a) CAD design of the stage; and (b) picture of the sample stage

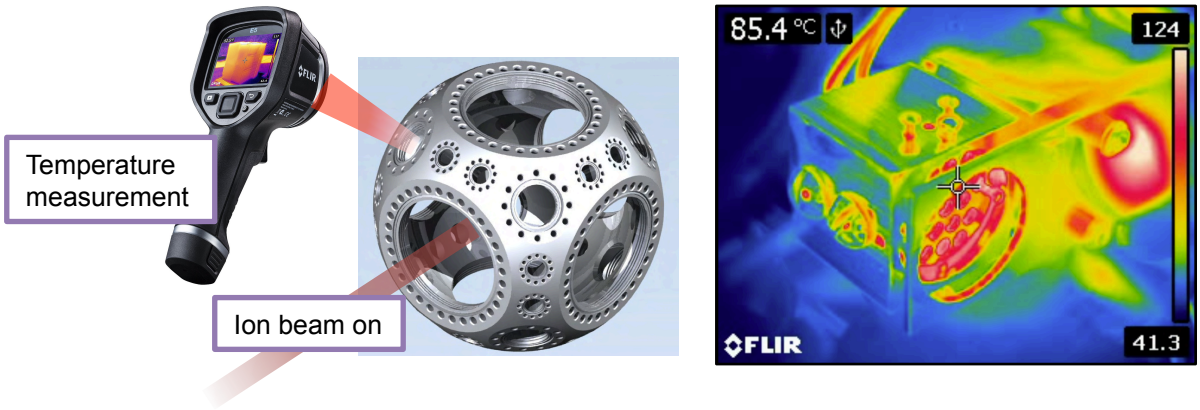

(a) (b)

Figure 7: (a) Scheme of the infrared camera measurement; and (b) an example of infrared imaging of temperature measurement

The final system set-up after sample loading is shown in Fig. 8. The rough pumping system is connected to the bottom port of the irradiation chamber to allow fast pumping and venting when changing samples. To better determine the ion current on the samples, we have employed three faraday cups placed at different positions in the system. The main faraday cup was placed about 1 meter upstream of the irradiation chamber. This faraday cup was used to determine the Gaussian beam shape, and to roughly estimate the ion-beam focus and size. An accurate beam current was determined from direct measurement on the sample itself, which was electrically insulated from the metallic chamber. In addition, a backup faraday cup was installed on a single axis manipulator. This faraday cup stayed at ~10 mm in front of the samples when fully inserted into the irradiation chamber.

A ceramic heater with maximum temperature of 1200ºC was installed and directly connected to the sample stage. The feed-though power outlet of the ceramic heater was connected to a temperature

controller (Omega). With a reading from a thermocouple attached to the sample, the closed-loop control of sample temperature was established.

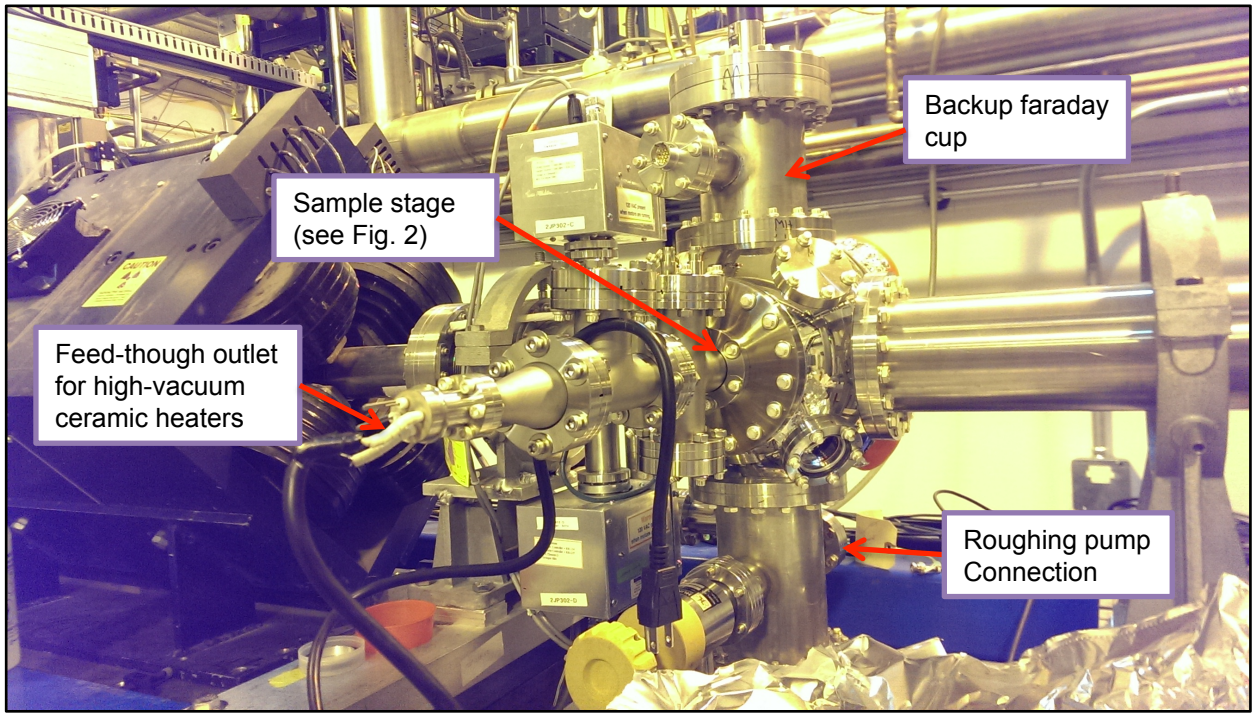

Figure 8: Irradiation chamber in the ATLAS

3.2 Sample Preparation and Irradiation Condition Determination

The large-grained UO_2 samples for Xe irradiations were fabricated at Rensselaer Polytechnic Institute (RPI). Fig. 9 shows scanning electron microscope (SEM) images of the UO_2 samples before irradiation. The grain size of the samples was measured to be 81 μm. These samples were sintered, doped with 0.5 wt% Ti. Some secondary phases were found in these large-grained UO_2 samples as the doping concentration was above the solubility limit of TiO_2 in UO_2. As a result, a eutectic phase (liquid phase) formed, promoting grain growth to very large sizes.

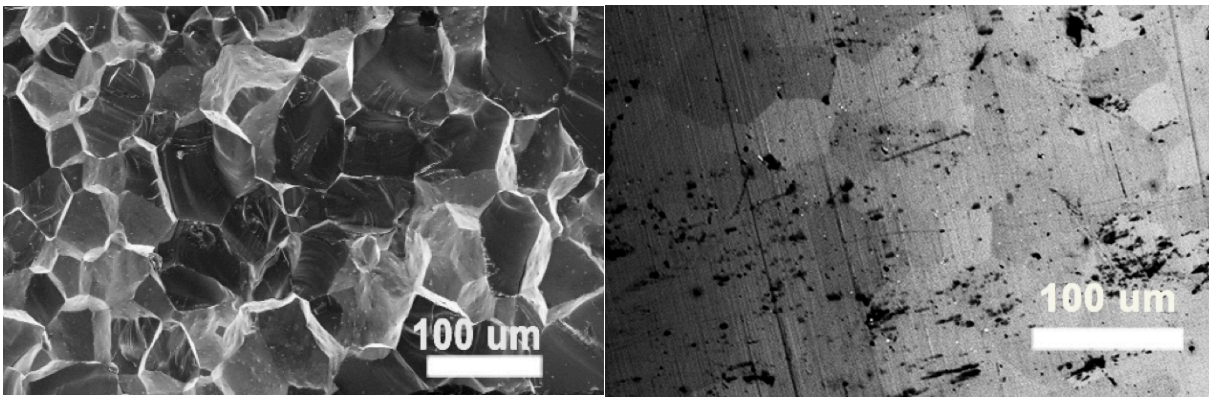

(a) (b)

Figure 9: Large-grained UO_2 samples for Xe irradiations at ATLAS: (a) the crystalline morphology; and (b) the polished sample surface

Four UO_2 samples were loaded into a sample stage which is capable of loading up to 19 specimens for simultaneous irradiation. The large-grained UO_2 samples were irradiated with 80MeV Xe ions. The ion beam profile was adjusted to be Gaussian-shaped with a full-width-half-maximum of 10 mm. The beam current was maintained to be 50 particle nano-Amperes (pna) during the experiment. The temperature of the sample during the irradiation was controlled to be ~150ºC. The final achieved dose was about 0.79×10^{17} ions/cm^2. A summary of irradiation conditions is given in Table 1.

Table 1: High-energy Xe implantation condition

Source	80 MeV Xe ions
Beam profile	Gaussian distribution
Beam width	FWHM = 10mm
Current	50 particle nano-Ampere
Irradiation time	56 hrs
Irradiation temperature	~ 150°C
Final dose on UO_2 samples	0.79×10^{17} ions/cm^2

According to SRIM calculation based on the given irradiation conditions, all the UO_2 samples achieved a peak damage of ~170 dpa and a peak Xe concentration of 8000 ppm. The high-energy irradiation produced a wide damage range from the surface to a depth of ~7 μm, whereas most of Xe atoms are concentrated in the region of ~4 to ~7 μm from the surface. The damage profile and the Xe concentration profile are given in Fig. 10 (a) and (b), respectively.

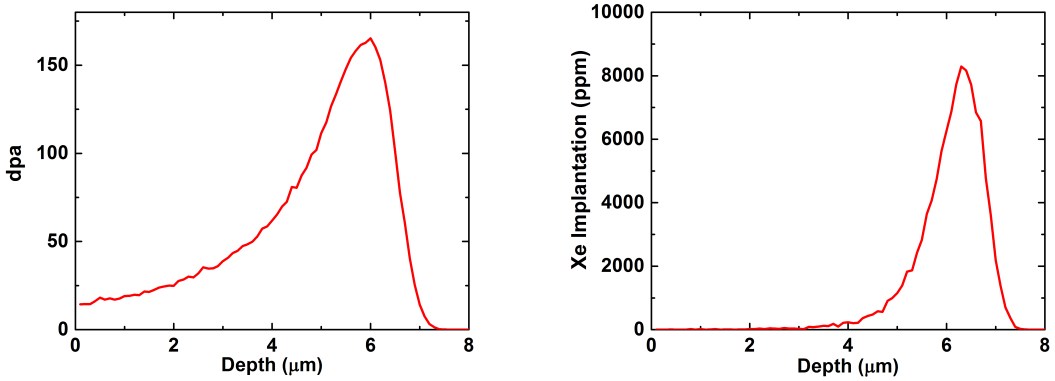

(a) (b)

Figure 10: (a) Damage profile in the unit of dpa; and (b) Xe concentration profile of large grained UO_2 samples

3.3 Plan for the Post-irradiation Examinations

After Xe implantation, the large-grained UO_2 samples were kept in a vacuum chamber to avoid possible oxidation. Post-irradiation annealing (PIA) and Post-irradiation examinations (PIEs) will be performed on these samples in FY16 to provide validation data for the MARMOT fission gas release model.

With ultra-high ion energy and relatively low sample temperature during irradiation, Xe ions were implanted into large-grained UO_2, and concentrated in the region about 6 μm from the surface exposed to radiations. Due to the relatively low intra-granular diffusivity of Xe, most implanted Xe ions were expected to be in the form of interstitial atoms or nano-scale bubbles within grains in UO_2. In order to develop a desired microstructure for PIEs, a PIA is needed to form relatively large intra-granular and larger inter-granular bubbles. The PIA temperature is estimated to be ~600ºC, and isothermal annealing time is ~1 hour, to allow Xe atoms to diffuse and develop desired bubble structures.

Following the annealing of the irradiated UO_2 samples, a series of PIEs are planned to investigate the gas bubble diffusion behavior in UO_2. The first key activity is focused ion beam (FIB)/ scanning electron microscopy (SEM) analysis. The SEM in the FIB is able to provide reasonable resolution of bubble structures. More importantly, the FIB is needed to fabricate TEM samples that can determine the bubble morphologies (for small to medium size bubbles) in different regions. Through both TEM and FIB/SEM examinations, two key features of the microstructure will be attained: (1) intra-granular and inter-granular bubble size and distribution; this is the foundation for later *in-situ* annealing experiments to promote Xe diffusion, and (2) bubble size and distributions on different types of grain boundaries; the TEM and FIB/SEM measurement will combine with the state-of-the-art micro-diffraction technique at APS to determine the impact of different grain boundaries on bubble morphology. With an X-ray probe of 400 nm × 500 nm, synchrotron micro-diffraction can provide 2D grain orientation mapping, allowing types of grain boundaries to be directly quantified. With the fully characterized microstructure of the UO_2 samples, *in-situ* TEM study will be conducted at the IVEM facility at ANL in order to directly observe the evolution of bubble structures as a function of temperature during isothermal annealing. In addition, if more samples are ready, *in-situ* irradiations at different temperatures will be performed for comparison to the *in-situ* TEM study with annealing alone. Hence, the impact of irradiation on Xe bubble diffusion will be determined. All the planned PIE activities are summarized in Table 2.

Table 2: Planned PIE analyses

Techniques	Purpose
SEM	Bubble structure investigation: medium and large size bubble characterization; TEM sample preparations
TEM	Bubble structure investigation: small and medium size bubble characterization
FIB/SEM	Synchrotron radiation sample preparations; *In-situ* TEM sample preparations
Synchrotron micro-diffraction	Grain orientation mapping to determine the types of grain boundaries
In-situ TEM (IVEM)	*In-situ* annealing/irradiation to see the evolution of bubble structure

4. Summary

This activity is supported by the US Nuclear Energy Advanced Modeling and Simulation (NEAMS) Fuels Product Line (FPL). Two major accomplishments in FY 15 are summarized in this report. The first one is the implementation of the FASTGRASS module in the BISON code. The coupled FASTGRASS module in BISON is capable of modeling LWR oxide fuel fission gas behavior and fission gas release. The formation and growth of fission gas bubbles in irradiated nuclear fuels is a process of vital technical importance because the behavior of these gas bubbles can have a significant impact on the swelling of the fuel, which may lead to fuel cladding failure during in-pile irradiation. In this report, the physics model of fission gas behavior and release in FASTGRASS is introduced; the rate theory formulation of the fission gas model is given in full detail. Because the BISON code structure is highly modular in C++ programming language, the FASTGRASS code was translated from its original Fortran 77 form to C++ and implemented into the BISON code as a module. The second accomplishment is a Xe irradiation experiment at ATLAS at ANL. This experiment aimed to produce required bubble structure in the large-grained UO_2 samples for further PIEs. The final goal of this effort is to provide validation data for the Fission Gas Release Model in MARMOT. To perform the irradiation experiment, a specially designed irradiation chamber was built and installed in the ATLAS beamline. An advanced sample holder, able to provide closed-loop temperature control and hold up to 19 samples for simultaneous irradiation within a single shot of ion beam, was built and used in the irradiation chamber for the Xe irradiation experiment on the UO_2 samples. High-energy Xe ions were successfully implanted in four large-grained UO_2 samples. The samples were subject to a dose of 0.79×10^{17} ions/cm^2 at a controlled temperature of approximately 150ºC. The peak damage region within the samples reached ~160 dpa, according to SRIM calculation based on the experimental conditions. All the irradiated UO_2 samples will be used in FY16 for post-irradiation annealing (PIA) and post-irradiation examinations (PIEs). PIA is planned to accelerate bubble formation in the samples. The PIEs will include FIB-SEM, TEM, and synchrotron X-ray micro-diffraction examinations.

5. Acknowledgements

This work was supported under US Department of Energy Contract DE-AC02-06CH11357. We would like to thank the MARMOT development lead, Michael Tonks, and MARMOT team member, Yongfeng Zhang, for providing very helpful guidance on this work.

6. References

1. H. Zimmermann, “Investigations on swelling and fission gas behavior in uranium dioxide,” Journal of Nuclear Materials, Vol. 75, pp. 154-161, (1978).

2. D. R. Olander, Fundamental aspects of nuclear reactor fuel elements, Technical Information Center, Office of Public Affairs, Energy Research and Development Administration, Chapter 12, 13, pp. 172-264, (1976).

3. T. Kogai, “Modeling of fission gas release and gaseous fuel swelling of light water reactor fuels,” Journal of Nuclear Materials, Vol. 244, pp. 131-140, (1997).

4. Y. S. Kim, G. L. Hofman, “Fission product induced swelling of U-Mo alloy fuel,” Journal of Nuclear Materials, Vol. 419, pp. 291-301, (2011).

5. J. Rest, “GRASS-SST: A Comprehensive, Mechanistic Model for the Prediction of Fission Gas Behavior of UO_2-base Fuels during Steady-state and Transient Conditions,” Argonne National Laboratory report, (1978).

6. J. Rest, “FASTGRASS: A Mechanistic Model for the Prediction of Xe, I, Cs, Te, Ba, and Sr Release from Nuclear Fuel under Normal and Severe-Accident Conditions,” Argonne National Laboratory report, NUREG/CR-5840, ANL-92/3 (1992).

7. B. Ye, J. Rest, “Assessment of the FASTGRASS fission-gas source term model in the Steady-state Regime,” ANL report 2010.

8. D. R. Olander, “Fundamental Aspects of Nuclear Reactor Fuel Elements,” (Energy Research and Development Administration, TID-26711-P1 (1976).

9. J. R. Matthews and M. H. Wood, “An efficient method for calculating diffusive flow to a spherical boundary,” Nucl. Eng. Des. 56, 439 (1980).

10. J. Rest, “The effect of irradiation-induced gas-atom re-solution on grain-boundary bubble growth,” J. Nucl. Mater. 321, 305 (2003).

11. J. Rest, “Evaluation of volatile and gaseous fission product behavior in water reactor fuel under normal and severe core accident conditions,” Nucl. Technol. 61, 33 (1983).

12. J. Rest, “An improved model for fission product behavior in nuclear fuel under normal and accident conditions,” J. Nucl. Mater. 120, 195 (1984).

13. K. Forsberg, A.R. Massih, Fission-Gas Release under Time-Varying Conditions, J Nucl Mater, 127, 141 (1985).

Nuclear Engineering Division
Argonne National Laboratory
9700 South Cass Avenue, Bldg. 208
Argonne, IL 60439

www.anl.gov

Argonne National Laboratory is a U.S. Department of Energy laboratory managed by UChicago Argonne, LLC